

## UvA-DARE (Digital Academic Repository)

### Discovery and Understanding of the Ambient-Condition Degradation of Doped Barium Cerate Proton-Conducting Perovskite Oxide in Solid Oxide Fuel Cells

Yan, N.; Zeng, Y.; Shalchi, B.; Wang, W.; Gao, T.; Rothenberg, G.; Luo, J.L.

#### DOI

[10.1149/2.0371514jes](https://doi.org/10.1149/2.0371514jes)

#### Publication date

2015

#### Document Version

Final published version

#### Published in

Journal of the Electrochemical Society

#### License

Article 25fa Dutch Copyright Act (<https://www.openaccess.nl/en/policies/open-access-in-dutch-copyright-law-taverne-amendment>)

[Link to publication](#)

#### Citation for published version (APA):

Yan, N., Zeng, Y., Shalchi, B., Wang, W., Gao, T., Rothenberg, G., & Luo, J. L. (2015). Discovery and Understanding of the Ambient-Condition Degradation of Doped Barium Cerate Proton-Conducting Perovskite Oxide in Solid Oxide Fuel Cells. *Journal of the Electrochemical Society*, 162(14), F1408-F1414. <https://doi.org/10.1149/2.0371514jes>

#### General rights

It is not permitted to download or to forward/distribute the text or part of it without the consent of the author(s) and/or copyright holder(s), other than for strictly personal, individual use, unless the work is under an open content license (like Creative Commons).

#### Disclaimer/Complaints regulations

If you believe that digital publication of certain material infringes any of your rights or (privacy) interests, please let the Library know, stating your reasons. In case of a legitimate complaint, the Library will make the material inaccessible and/or remove it from the website. Please Ask the Library: <https://uba.uva.nl/en/contact>, or a letter to: Library of the University of Amsterdam, Secretariat, Singel 425, 1012 WP Amsterdam, The Netherlands. You will be contacted as soon as possible.

UvA-DARE is a service provided by the library of the University of Amsterdam (<https://dare.uva.nl>)



## Discovery and Understanding of the Ambient-Condition Degradation of Doped Barium Cerate Proton-Conducting Perovskite Oxide in Solid Oxide Fuel Cells

Ning Yan,<sup>a,b,\*</sup> Yimin Zeng,<sup>c</sup> Babak Shalchi,<sup>c</sup> Wei Wang,<sup>a</sup> Tong Gao,<sup>a</sup> Gadi Rothenberg,<sup>b</sup> and Jing-li Luo<sup>a,\*</sup>

<sup>a</sup>Department of Chemical and Materials Engineering, University of Alberta, Edmonton, Alberta T6G 2V4, Canada

<sup>b</sup>Van't Hoff Institute for Molecular Sciences (HIMS), University of Amsterdam, Amsterdam 1098XH, The Netherlands

<sup>c</sup>CanmetMATERIALS, Natural Resources Canada, Hamilton, Ontario L8P 0A5, Canada

Proton-conducting perovskite oxides such as doped barium cerate and barium zirconate are promising electrolytes for solid oxide fuel cells (SOFCs). Here we report that the typical high performance proton conductor, BaZr<sub>0.1</sub>Ce<sub>0.7</sub>Y<sub>0.2</sub>O<sub>3±δ</sub> (BZCY), is prone to physical, chemical and thereby electrochemical degradations as it ages under ambient conditions. This aging effect destroys the electrolyte disk and breaks down the perovskite lattice. Electrochemical measurements indicate degraded BZCY based SOFC suffers from significant performance losses, and various advanced materials characterization results confirm that this degradation of BZCY is exclusively caused by water and CO<sub>2</sub> from the surrounding environment. The water molecules catalyze the degradation, initiating and promoting the carbonation of BZCY. The subsequent reaction with CO<sub>2</sub> creates two major phases: BaCO<sub>3</sub> nano-rod single crystals and amorphous oxide mixtures. The entire process is visualized via TEM observations, based on which we propose that this occurs via the microcrucible mechanism. As this mechanism does not incur significant segregations of decomposition products, the aged BZCY powder is easily regenerated by re-calcination. We then study the effects of doping on the stability of BZCY, showing that a higher Zr content obviously improves the aging resistance.

© 2015 The Electrochemical Society. [DOI: 10.1149/2.0371514jes] All rights reserved.

Manuscript submitted September 9, 2015; revised manuscript received September 28, 2015. Published October 6, 2015.

Although generating power from renewable sources is high on the wish list of practically all governments, fossil fuels will remain our chief source of power in the next decades.<sup>1</sup> Even so, we can still benefit much by optimizing our power-generation methods, thus reducing CO<sub>2</sub> emissions and increasing efficiency. One way to do this is using fuel cell technology,<sup>2</sup> because fuel cells are inherently more efficient than internal combustion engines. In particular, solid oxide fuel cells (SOFC) are promising for power generation applications.<sup>3–6</sup> Much research has been devoted to optimizing cell configurations, electrode-catalysts, and electrolyte materials.<sup>7–10</sup> Among all the solid-state electrolyte candidates, the proton-conducting perovskite oxide, barium cerate (BaCeO<sub>3</sub>), is advantageous since it has a relatively high ionic conductivity at intermediate temperature ( $\sim 10^{-2}$  S cm<sup>-1</sup> at 700°C), which is much lower than the temperatures requires for oxide-conducting membranes.<sup>11</sup> Moreover, using a proton-conducting SOFC configuration enhances the efficiency, since the water is generated at the cathode side and does not dilute the fuel.<sup>12</sup> To further improve the protonic conductivity, acceptor-doping of cerate, e.g., using Y<sup>3+</sup>, Nd<sup>3+</sup>, Gd<sup>3+</sup>, and Yb<sup>3+</sup>, is employed to generate more oxygen vacancies,<sup>13</sup> facilitating the formation of higher concentration of protonic defects.<sup>11,14–18</sup> Yttrium is known as one of the most suitable for the cerium substitution.

Despite these promising characteristics, aliovalent-doped BaCeO<sub>3</sub> is unstable at the SOFC operating temperatures, it suffers from kinetically and thermodynamically favorable reactions with water vapor and/or CO<sub>2</sub> at elevated temperatures, hampering its practical applications.<sup>19,20</sup> In contrast, BaZrO<sub>3</sub>-based materials, another series of proton conductors, are more stable,<sup>21</sup> albeit with relatively poor conductivity.<sup>22,23</sup> Fortunately, the BaCeO<sub>3</sub>-BaZrO<sub>3</sub> solid solution combines the advantages of both: good stability and sufficient conductivity.<sup>24</sup> In particular, 10 mol% Zr doped cerate, e.g., BaZr<sub>0.1</sub>Ce<sub>0.7</sub>Y<sub>0.2</sub>O<sub>3±δ</sub> (BZCY), shows high conductivity and resists both concentrated CO<sub>2</sub> and water vapor.<sup>17,25,26</sup> Satisfactory SOFC performances were also broadly documented using BZCY or additional dopants-optimized BZCY electrolyte.<sup>17</sup>

Notwithstanding these high-temperature results, the stability of the electrolyte materials under ambient conditions is equally important,<sup>27</sup> as it impacts the storage, transportation and installation of SOFC systems. Thermodynamically, both cerate and zirconate are more prone

to decomposition at lower temperatures. But few studies examine their stability at room temperature under atmospheric CO<sub>2</sub> and humidity conditions. This seems logical, as intuitively one would imagine that such robust materials that show good stability at high temperatures would react very slowly, if at all, under ambient conditions.<sup>19,28</sup> But BZCY is an exception. As we show here for the first time, it undergoes destructive aging degradation when exposed to simple ambient air at room temperature (<0.04% CO<sub>2</sub> and <35% relative humidity). In this paper, we explore the source, visualize and explain the mechanism of this degradation from the nanoscale, and show how it can be reversed and even avoided.

### Experimental

**Materials and instrumentation.**— X-ray diffraction (XRD) patterns were recorded using a Rigaku Geigerflex powder diffractometer equipped with a cobalt tube. X-ray photoelectron spectroscopy (XPS) was measured using a Kratos Analytical AXIS 165, in which a monochromated Al K $\alpha$  (h $\nu$  = 1486.6 eV) source was used under the pressure of  $3 \times 10^{-8}$  Pa. Fourier transform infrared (FTIR) spectra were measured on a Nicolet 8700 spectrometer. Thermogravimetric and differential scanning calorimetry analyses (TGA-DSC and TGA-MS) were run on a TA Instruments SDT Q600 coupled with a thermostat QMS 200 mass spectrometer. The temperature ramp rate was 10°C min<sup>-1</sup>. Electrochemical measurements were done using a Solartron 1287 potentiostat with a 1255 frequency response analyzer.

The morphology of samples was characterized using a Keyence VHX-5000 digital optical microscope. Detailed microstructures were obtained using a JAMP-9500F field emission scanning electron microscope (FE-SEM). Transmission electron microscope (TEM) samples were prepared by spreading small amount of powders onto the copper grid, which were then studied under the electron beam using a Tecnai Osiris microscope operating at 200 kV equipped with a high angle annular dark field (HAADF) detector and an electron energy loss spectrometer (EELS). ChemiSTEM X-ray detection technology and Energy-dispersive x-ray spectroscopy (EDS) were used to study the chemistry of different phases, via quantitative analysis and elemental mapping.

**Procedure for preparing BZCY nano-powders.**— A version of this procedure was published in our earlier work.<sup>12</sup> First, 0.06 mmol citric acid, a chelating agent, was diluted in 100 ml deionized

\*Electrochemical Society Active Member.

<sup>z</sup>E-mail: jingli.luo@ualberta.ca; n.yan@uva.nl

water, and then stoichiometric amounts of metal nitrate precursors (0.02 mmol  $\text{Ba}(\text{NO}_3)_2$ , 0.014 mmol  $\text{Ce}(\text{NO}_3)_3 \cdot 6\text{H}_2\text{O}$ , 0.004 mmol  $\text{Y}(\text{NO}_3)_3 \cdot 6\text{H}_2\text{O}$  and 0.002 mmol  $\text{ZrO}(\text{NO}_3)_2 \cdot 4\text{H}_2\text{O}$ ) were added at a 3:2 molar ratio of citric acid : total metal ions. Finally, appropriate amount of  $\text{NH}_4\text{NO}_3$  was added to the solution as the fuel and the pH was adjusted to  $\sim 8$  using ammonium hydroxide. The solution was heated on the hot plate until self-combustion occurred, and the powder was then calcined at  $1200^\circ\text{C}$  for 10 h to give the pure perovskite phase.  $\text{BaCe}_{0.8}\text{Y}_{0.2}\text{O}_3$  (BCY) and  $\text{BaZr}_{0.8}\text{Y}_{0.2}\text{O}_3$  (BZY) were synthesized similarly.

**Procedure for electrochemical studies.**— In the preparation of the BZCY electrolyte pellet, the calcined nano-powder was grinded in alcohol, dried and pressed into thick discs ( $\sim 0.8$  mm thick, 19.05 mm in diameter) which were densified via sintering in air at  $1450^\circ\text{C}$  for 10 h. To avoid the evaporation of BaO, the disc was fully covered with fine BZCY powders during densification process, which had been proven as an effective way of minimizing the surface depletion of Ba. The membrane electrolyte assembly (MEA) was fabricated via applying Pt paste on both sides of BZCY disc. The natural degradation test, using both BZCY powder and discs, was carried out at room temperature ( $21^\circ\text{C}$ ) in ambient air with atmospheric  $\text{CO}_2$  (0.04 vol.%) and minor moisture (RH < 35% which equals to  $\sim 0.11$  vol.%  $\text{H}_2\text{O}$  vapor). In the accelerated degradation test, BZCY discs were placed in a sealed quartz tube with either dry or humidified ( $\sim 0.3$  vol.%  $\text{H}_2\text{O}$ ) gases passing through at a flow rate of  $50 \text{ ml min}^{-1}$  for 24 h.

## Results and Discussion

**Degradation of electrochemical performance.**— In a typical electrochemical test, the BZCY electrolyte was incorporated into an electrolyte-supported SOFC button cell. The pristine Pt/BZCY/Pt button cells showed reasonable and highly repeatable electrochemical performances. However, this performance worsened for the cells after prolonged storage under ambient conditions. Figure 1 shows a typical example of this performance loss in which three distinct cells have been treated differently. In the polarization and power density plots in Figure 1a, the pristine Pt/BZCY/Pt cell showed a maximum power density of  $\sim 180 \text{ mW cm}^{-2}$ . For another cell (cell *1 week A* which was stored in a beaker exposed to the ambient air with relative humidity, RH =  $(35 \pm 7)\%$  for a week at  $21^\circ\text{C}$ ), the power density dropped to  $\sim 160 \text{ mW cm}^{-2}$ . To further evaluate the influence of humidity on the electrochemical performance, an additional control cell was kept in a desiccator for a week at  $21^\circ\text{C}$  (cell *1 week B*, instead of loading desiccant, we added saturated KI solution to keep the relative humidity at 68%). Here, more significant degradation was observed in comparison to cell *1 week A*: the maximum power density decreased drastically to  $\sim 90 \text{ mW cm}^{-2}$ .

Figure 1b shows the corresponding impedance spectra. Compared with the pristine cell, both the ohmic and charge transfer resistances of cell *1 week A* increased slightly and this increase was substantially more noticeable for cell *1 week B*. As the ohmic resistance is simply related with the electrical properties of the cell, we assumed that due to the moisture, new phases with higher resistance formed in both of the cells. Normally, the charge transfer resistance represents the catalytic properties of the triple-phase boundary (TPB). Its growth implied the deterioration of Pt-BZCY interfaces, correlating with the formation of higher resistance phases on the surface of BZCY.

**Physical and chemical degradation of a BZCY electrolyte disc.**— The electrochemical tests results in Figure 1 show that humidity played a vital role in the degradation of the Pt/BZCY/Pt cell in ambient air. To study the physico-chemical changes further, we ran an accelerated aging experiment on densified BZCY electrolyte discs, using a humidified air feed stream (RH = 100%) for 24 h at  $21^\circ\text{C}$ . The degradation was examined using sequential optical microscopy and FE-SEM. Prior to the humidified air treatment, the disc surface was smooth, with relatively high mechanical strength and no Ba depletion (see Figures 2a and 2c). It was well-densified, with the grain boundaries clearly

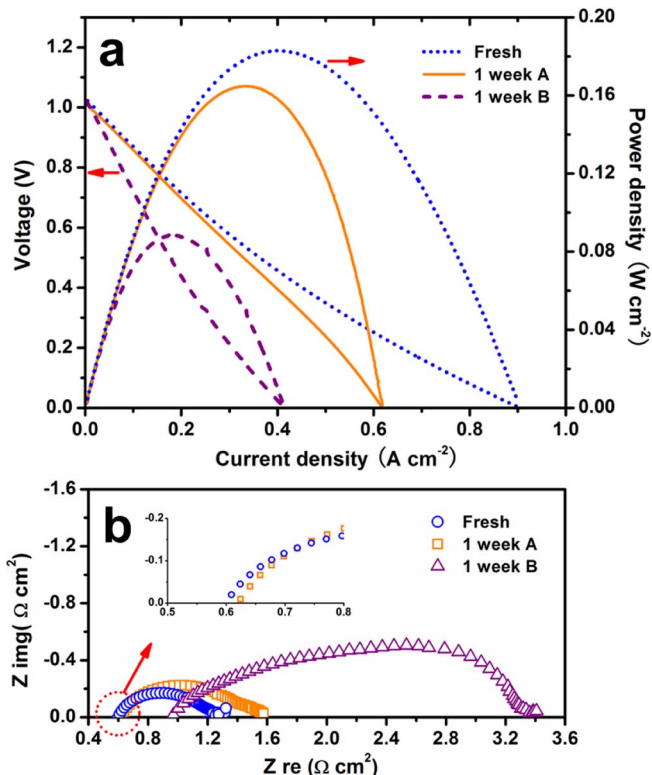


**Figure 1.** SOFC performances of different cells with the same Pt/BZCY/Pt configuration in  $\text{H}_2$  at  $700^\circ\text{C}$ . (a) polarization and power density plots; (b) impedance spectra of the corresponding cells.

observed showing no micro-holes or -cracks. But after the exposure (Figure 2b), the disc became extremely fragile, losing its structural integrity completely (it fell to pieces under gentle finger pressure). The FE-SEM image in Figure 2d pertains to the fragments shown in Figure 2b. The microstructure of BZCY has changed dramatically: grain boundaries were blurred, and many rod-like nanostructures appeared, deposited on the surface of much larger particles (see the inset).

X-ray diffraction was used to identify the secondary phases in the degraded BZCY samples and to understand how these formed at

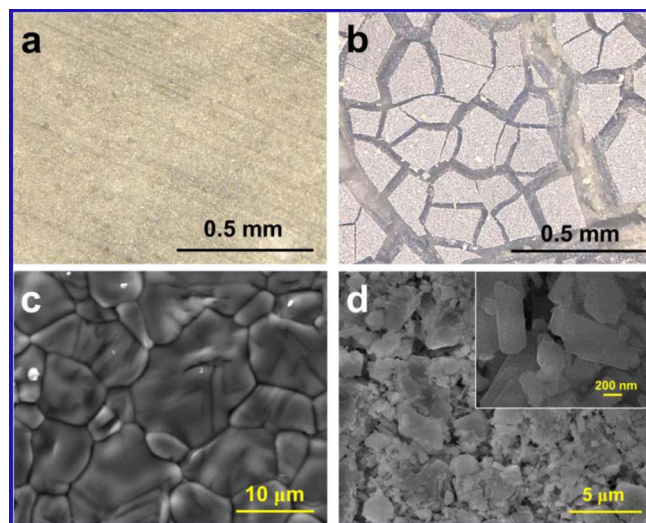


**Figure 2.** Optical and FE-SEM images of BZCY disc sample (a, c) before and (b, d) after exposure to humidified air feed steam (RH = 100%) for 24 h at  $21^\circ\text{C}$ .

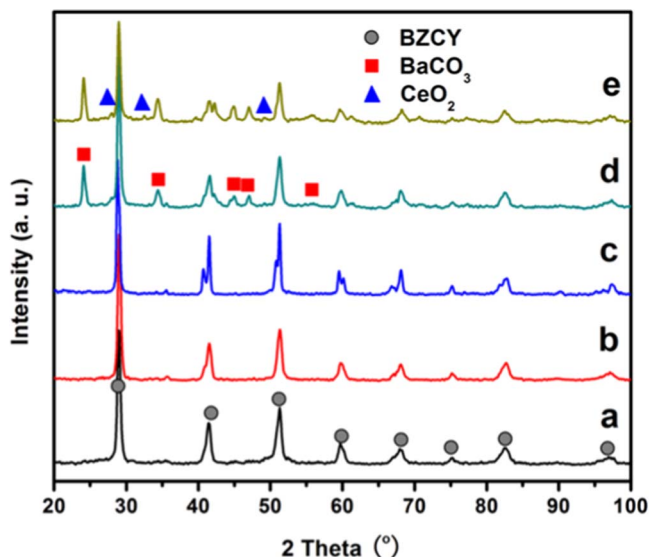
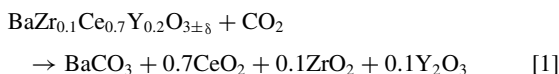
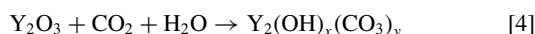


**Figure 3.** X-ray diffraction patterns of BZCY under different degradation conditions for 24 h at 21°C: (a) pristine BZCY, (b) BZCY in dry air, (c) BZCY in dry CO<sub>2</sub>, (d) BZCY in humidified air (RH = 100%), (e) BZCY in humidified CO<sub>2</sub> (RH = 100%).

room temperature. The pristine BZCY sample was stable in both dry air and dry CO<sub>2</sub>, showing no impurity peaks (see Figure 3). However, when moisture was added to the feed streams, the sample partially decomposed, giving BaCO<sub>3</sub> and CeO<sub>2</sub>. As the doping ratios of zirconium and yttrium at the ‘B’ site of the perovskite were only 10% and 20%, respectively, their decomposition products could not be identified through XRD. Equation 1 shows one possible decomposition reaction:



Since Y<sub>2</sub>O<sub>3</sub> is hygroscopic, the final form of the yttrium compound in the degraded sample can vary considerably.<sup>29,30</sup> The yttrium might be present as a hydroxide, a carbonate, a hydroxycarbonate or an oxycarbonate (Equation 2–5). The actual composition of the yttrium compounds in the degraded BZCY sample was characterized using XPS and FTIR (see below). Nevertheless, it was clear that the combination of moisture and CO<sub>2</sub> caused this decomposition.



TEM measurements were then carried out to characterize the nano-rod structures formed during the degradation. The rods’ thickness varied between 50–300 nm based on the bright-field image shown in Figure 4a. Moreover, the selected area electron diffraction (SAED) pattern in Figure 4b suggests that the nano-rod is a BaCO<sub>3</sub> single crystal viewed from the [510] direction. This assignment was further supported by the dark-field micrograph shown in Figure 4c that was taken from the (002) reflection of BaCO<sub>3</sub> in the SAED pattern. The single-crystal formation was also confirmed by HRTEM (Figure 4d) which shows only one crystallographic orientation. We thus concluded that the degradation of BZCY led to the formation of BaCO<sub>3</sub> single-crystal nanorods.

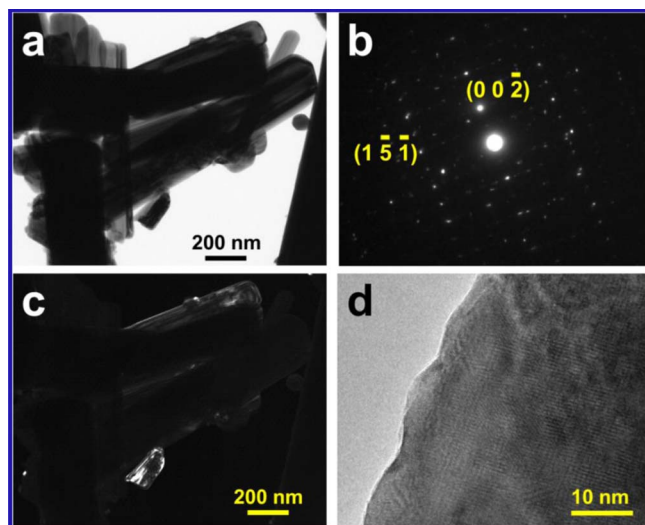


**Figure 4.** TEM images of the BaCO<sub>3</sub> nano-rod structure in the degraded BZCY sample: (a) bright-field image, (b) selected area electron diffraction (SAED) pattern, (c) dark-field image taken from the (002) reflection of BaCO<sub>3</sub>, and (d) HRTEM image from the near surface area of a BaCO<sub>3</sub> nano-rod.

Subsequently, we ran thermal analyses on both the pristine and the degraded samples (Figures 5a and 5b, respectively). The thermogravimetric analysis (TGA) show that the weight of the pristine BZCY sample was stable up to 1300°C. The associated 3 wt% weight loss reflected the non-stoichiometric oxygen difference in the lattice at high temperatures.<sup>31</sup> The smooth DSC curve also precluded major physical or chemical changes. Conversely, the degraded sample showed four stages of weight loss, corresponding to endothermic peaks in the DSC curve. The first, at ca. 100°C, pertained to water evaporation. The other three stages showed also strong CO<sub>2</sub> signals in the TGA-MS of the effluent (Figures 5b and 5c, the signal was delayed to 400–1220°C due to retention time). Thus, those weight changes probably arose from the decomposition of carbonates. A control experiment using pure BaCO<sub>3</sub> confirmed that its decomposition temperature was higher than 900°C, in agreement with published data.<sup>32</sup> According to the decomposition temperature reported elsewhere,<sup>33,34</sup> the second and third stages of weight loss are likely due to the two-step decomposition of (hydrated) hydroxycarbonate, Equation 6,



The presence of yttrium hydroxycarbonate was further confirmed by XPS and by FTIR spectroscopy. Figure 6a shows the yttrium 3d core level high resolution X-ray photoelectron spectra of the degraded BZCY sample, with an overlap of the 3d<sub>5/2</sub> and the 3d<sub>3/2</sub> core electrons. The peaks with binding energies of 155.8 eV and 157.7 eV for the Y 3d<sub>5/2-3/2</sub> doublet were assignable to the doped Y in BZCY.<sup>35</sup> The other peak pair had a positive chemical shift, implying that the Y atoms have bonded to more electronegative groups. This agreed with the formation of yttrium hydroxycarbonate which was known to have positive chemical shifts compared with yttrium oxide.<sup>36</sup> Similarly, in the C 1s spectrum (Figure 6b), besides the adventitious carbon that linked with the binding energy of 285 eV, the high binding energy sections indicated additional species, including C–O–C and C–O–H at 286.5 eV, C=O, O–C=O and CO<sub>3</sub><sup>2-</sup> between 288–290 eV,<sup>37</sup> all supporting the formation of hydroxycarbonate in degraded BZCY sample.

The FTIR spectra shown in Figure 7 also confirm the presence of carbonate species. In the spectrum of pristine BZCY, the broad band between 3000–3600 cm<sup>-1</sup> represented the stretching vibration mode of the water O–H bond. The other notable peak located at ~1400 cm<sup>-1</sup> pertained to minor carbonate species, originating from the degradation of pristine BZCY sample during its transfer to XPS chamber. In the spectrum of degraded BZCY, another band attributable to the

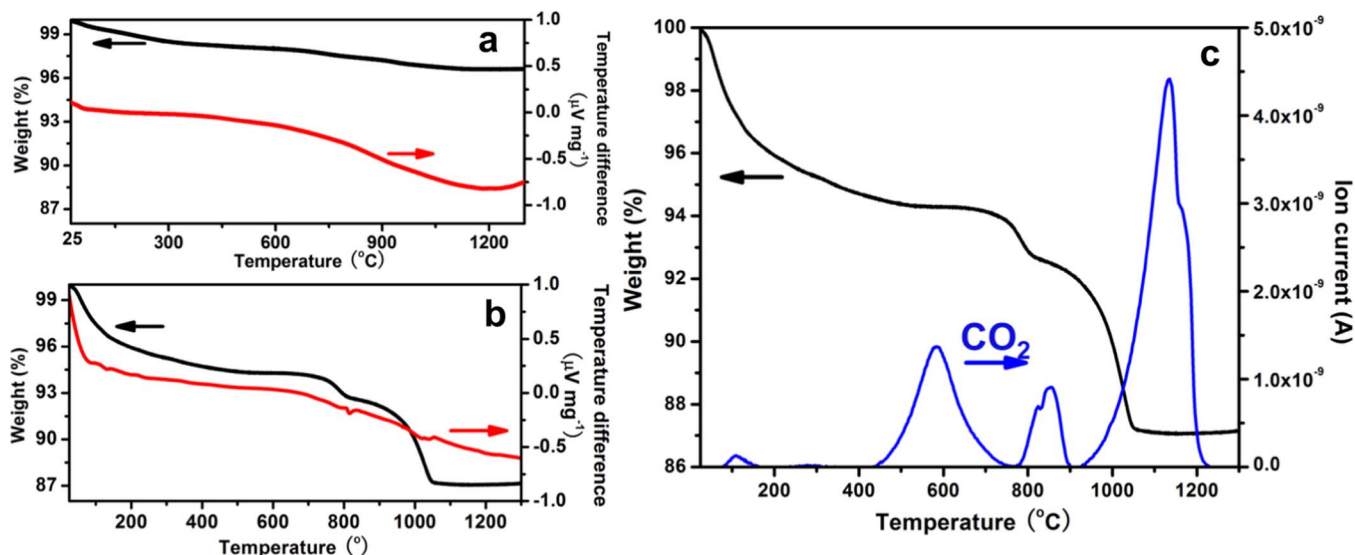


**Figure 5.** TGA-DSC curves of (a) pristine BZCY and (b) degraded BZCY; and TGA-MS curves of (c) degraded BZCY, the  $\text{CO}_2$  in the effluent was analyzed by mass spectrometry.

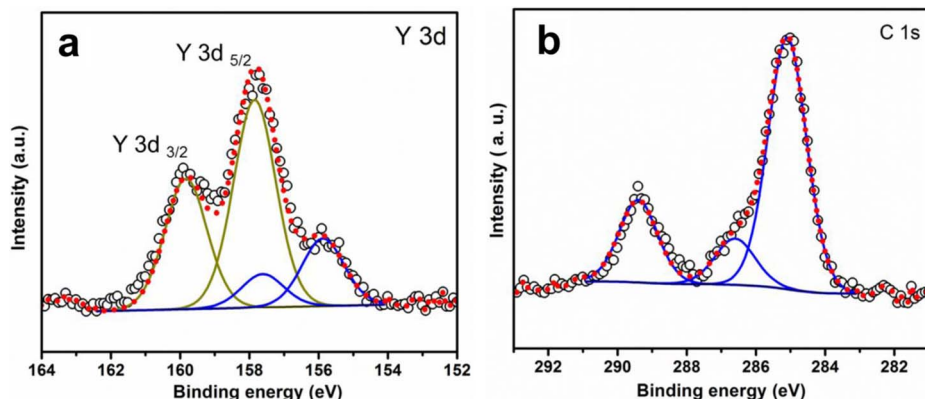


**Figure 6.** The core-level high resolution XPS spectra showing the yttrium 3d and carbon 1s in the degraded BZCY sample.

stretching and bending mode of hydroxyl group was prominent at  $1075\text{ cm}^{-1}$ .<sup>33</sup> The intensity of the carbonate peak at approximately  $1400\text{--}1500\text{ cm}^{-1}$  was substantially higher suggesting that more carbonates formed. Several additional peaks between  $700$  and  $2500\text{ cm}^{-1}$  in the degraded sample were all assignable to the formation of carbonates.<sup>30</sup>

Analogous to the formation of  $\text{BaCO}_3$ , the crystallization and growth of yttrium hydroxycarbonate could lead to the segregation of yttrium out of the matrix phase in the degraded BZCY sample. Transmission electron microscopy (TEM) analysis showed Y-enriched phases, supporting the presence of yttrium hydroxycarbonate. Figure 8a is a TEM image of two  $\text{BaCO}_3$  nano-rods growing from BZCY matrix. This was confirmed by the elemental mapping data shown in Figures 8b–8e. Interestingly, the analysis showed a yttrium-rich stripe within the nano-rod. This enriched phase was also noticeable in Figure 8a (indicated by the arrow). As neither Ce nor Zr was detected within this square area, this heterogeneity implied an uphill diffusion and segregation of the Y species from the originally uniform oxide.<sup>38</sup> The driving force for this was the chemical potential change during the crystallization of the new compound, yttrium hydroxycarbonate.

*Effects of doping elements and degradation reversibility.*— To examine the effect of dopants over the stability of BZCY against aging degradation, BZY and BCY samples were also exposed to humidified air stream ( $\text{RH} = 100\%$ ) for 24 h at room temperature. The diffraction patterns shown in Figure 9a reveal that both samples contained  $\text{BaCO}_3$  impurities after the treatment. However, the degradation of BCY was

much more pronounced. We therefore concluded that (i) yttrium-doped barium cerate, and likely barium zirconate too, was vulnerable to the degradation in humid air at room temperature. This was also supported by the thermodynamic calculations. In fact, zirconate was

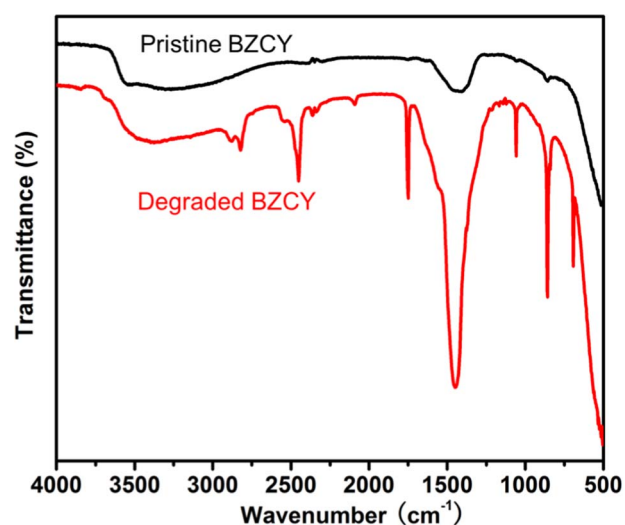


**Figure 7.** FT-IR spectra of (a) the pristine and (b) the degraded BZCY sample.

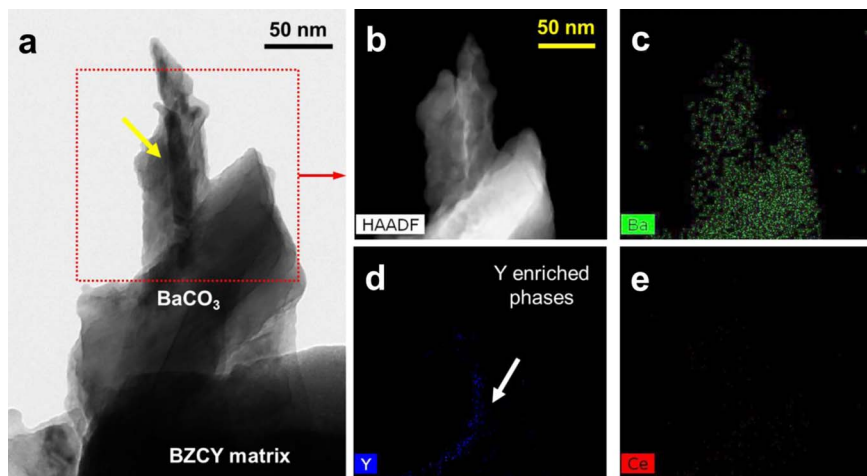


**Figure 8.** TEM analysis of  $\text{BaCO}_3$  and  $\text{Y}_2(\text{OH})_2(\text{CO}_3)_2$  from degraded BZCY sample: (a) BF image, (b) HAADF image of the square area in (a), (c–e) EDX elemental mapping within the area shown in (b).

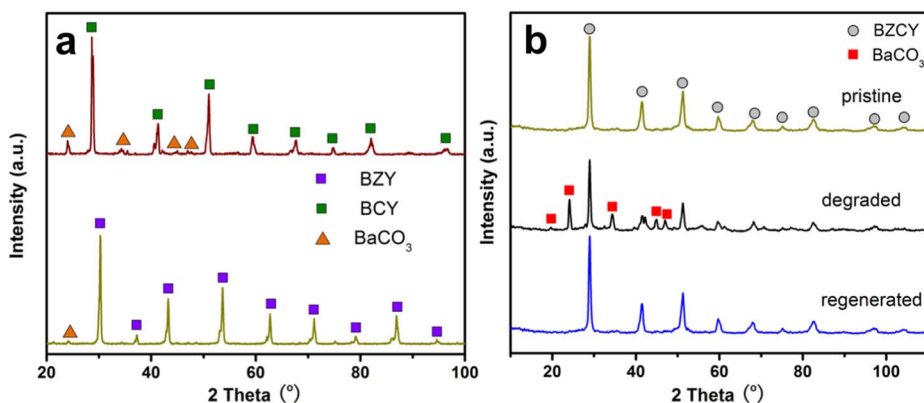


**Figure 9.** XRD patterns of (a) BZY and BCY after exposure to humidified air (RH = 100%) for 24 h at room temperature; (b) Three BZCY samples: pristine, degraded in humidified air (RH = 100%) for 24 h at room temperature, and regenerated at 1200°C for 10 h.

widely documented as steam and atmospheric  $\text{CO}_2$  resistant at typical SOFC working temperatures,<sup>23,24</sup> more work needs to be done to fully understand the origin of the tiny amount of impurities in the treated BZY sample; and (ii) a higher Zr doping ratio slowed down the aging degradation of BZCY.

The diffraction patterns in Figure 9b show that the degradation process is reversible. After 24 h in humidified air, the partially decomposed BZCY powder was not re-mixed or re-homogenized, but directly re-calcined at 1200°C for 10 h, which surprisingly returned a pure BZCY perovskite. This full regeneration had important practical

implications for SOFC manufacturing, as the high-temperature sintering step during the fabrication can remedy any earlier decomposition of the electrolyte.<sup>39</sup>

*The degradation mechanism.*— To understand the BZCY degradation process and mechanism, we must look at how the  $\text{BaCO}_3$  nano-rod single crystal formed. Visualization of the compositional as well as the morphological changes of BZCY during the aging provides an powerful way to explore it from nanoscale.<sup>40,41</sup> Interestingly, all of the nanorods observed in TEM images (see Figures 4a, 4d and 10a)

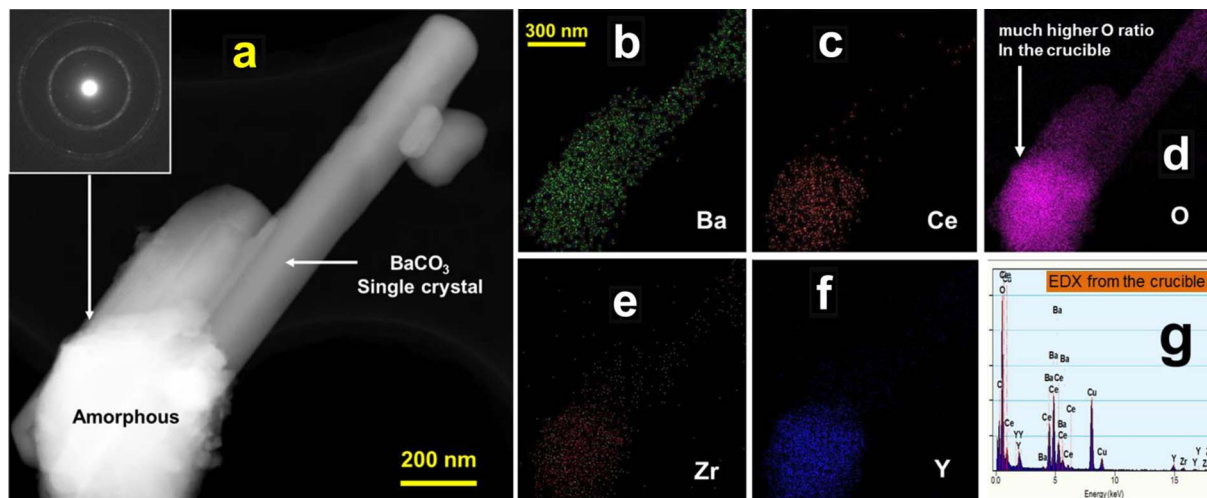


**Figure 10.** TEM analysis of degraded BZCY sample: (a) HAADF image with SAED inset, (b–f) EDX elemental mapping micrographs of the sample shown in (a), and (g) EDX spectrum obtained from the amorphous crucible.

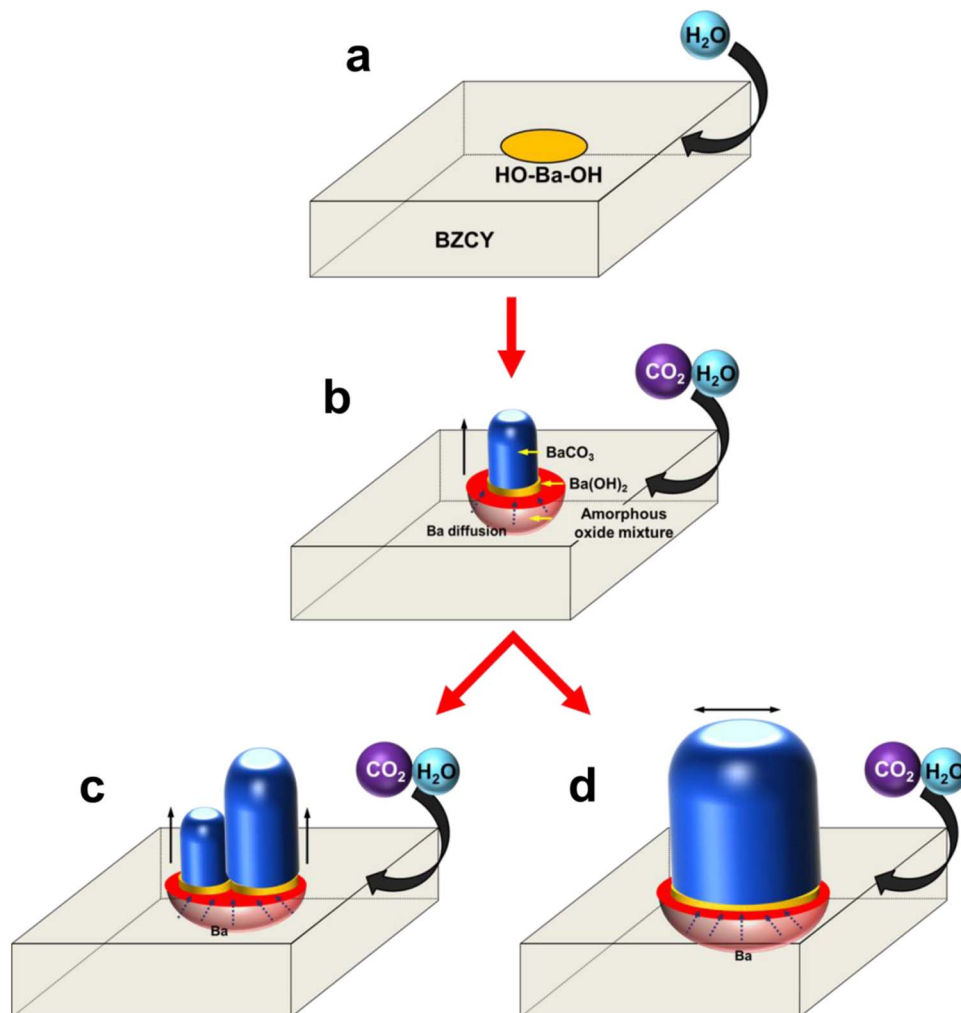


**Figure 11.** A schematic of BZCY degradation mechanism in ambient air at room temperature.

had sharply faceted ends and uniform cross-sections. They were extruded from the underlying BZCY matrix, causing the collapse of the perovskite crystals and the formation of a crucible-like structure at the bottom of the nanorod (see Figure 10a). The SAED pattern (Figure 10a, inset) indicates that this crucible was amorphous, and the EDX mappings show that all Y, Zr and Ce species were constrained within this region. This indicated that, in addition to the formation of BaCO<sub>3</sub> single crystals, the decomposition of BZCY also led to the formations of amorphous ZrO<sub>2</sub> and CeO<sub>2</sub> (cf. the broad and weak peak of CeO<sub>2</sub> in the diffraction pattern in Figure 3).

Based on these observations, we suggested that the aging decomposition of BZCY followed a microcrucible mechanism.<sup>42,43</sup> In this process, a liquid and a solid phase coexisted: the liquid phase dissolved Ba ions out of the solid matrix, forming a crucible-shaped structure underneath. The new BaCO<sub>3</sub> phase then grew from this ion-rich liquid region. The liquid phase in this case was hydrated Ba(OH)<sub>2</sub>, the BZCY decomposition intermediate in the presence of H<sub>2</sub>O,<sup>19,20</sup> that strongly attracted water molecules from the surrounding air. This hypothesis was supported by the extremely high atomic ratio of oxygen (89.1 atom %, note that hydrogen cannot be detected) in the amorphous crucible zone from quantitative EDX and EELS data (see Figure 10d). The presence of the shoulder band at 1600 cm<sup>-1</sup> in the FTIR spectrum (Figure 7) also revealed the existence of free water molecules in the sample.<sup>33</sup> Without water, no liquid phase could form, and indeed BZCY was perfectly stable in both dry air and dry CO<sub>2</sub> atmosphere (see Figure 3).

Figure 11 shows a cartoon of the degradation mechanism. It is initiated by sorption of water and the subsequent formation of hydroxide liquid solution on the surface (Figure 11a).<sup>20</sup> In the presence of CO<sub>2</sub>, the hydroxide was reacted to give BaCO<sub>3</sub>, which grew as a nanorod with essentially an identical diameter as the liquid spot as shown in Equation 7.



In consideration of the presence of protonic defects in BZCY, the hydroxide might form initially at the oxygen vacancy sites,<sup>44</sup> the reaction is shown in Equation 8 following the Kröger-Vink notation:



Meanwhile, the extrusion of Ba compound and the formation of extra water (Equation 7) readily caused the dilution of Ba ions in the liquid solution, driving more barium ions underneath to dissolve. The Ba-depleted zone in the underlying BZCY substrate would gradually form a crucible-like structure (see Figure 11b). With the continuous leaching of Ba ions from the BZCY lattice, the perovskite complex oxide would be finally destructed to form a crucible filled of simple oxides mixture. Due to the low temperature, the oxides did not crystallize (cf. the amorphous phase shown in Figure 10a). Accordingly, the microcrucible provided an effective diffusion pathway of Ba ions to the liquid phase, enabling the epitaxial growth of the BaCO<sub>3</sub> single-crystal and eventually the nano-rod formation.

During the degradation, the liquid phase, interface and underlying solid microcrucible formed simultaneously. This complex dynamic process enabled the morphological alternations of BaCO<sub>3</sub> nanorod. Our TEM results showed two distinct morphologies. The first is shown in Figure 11c representing two joined nanorods, formed either by merging two adjacent microcrucibles or via the formation of a new BaCO<sub>3</sub> nucleation site within the same microcrucible. An example of this morphology with a ‘stepped end’ is shown in Figure 10a. The second is a single long and ‘fat’ nanorod (Figure 11d) suggesting the nanorod can grow in both width and length directions.<sup>43</sup> This can explain the varied diameters of the nanorods in Figure 4a.

In general, the degradation process of BZCY in ambient air at room temperature involved a synergistic effect of CO<sub>2</sub> and H<sub>2</sub>O. The key reactions here were determined as the formation of carbonates (see Equation 1), though the subsequent formation of Y<sub>2</sub>(OH)<sub>2</sub>(CO<sub>3</sub>)<sub>2</sub> might coexist (see Equation 4). The doping elements, such as Zr, have been proven to be able to increase the stability of cerate against decomposition. Their segregations near the grain boundary regions and the resulting space charge effect rendered these regions less-vulnerable to the degradation.<sup>45,46</sup> Accordingly, rather than proceeding from the grain boundary defects, the decomposition started from the bulk cerate grain, where the minor depletion of dopant might occur. This caused intragranular fractures and ultimately the loss of mechanical integrity (cf. the degraded BZCY sample in Figure 2d).

### Conclusions

Although the proton-conducting BZCY electrolyte is stable and robust at the high temperatures of SOFC operation, it degraded in ambient air at room temperature. This abnormal process was actually a reaction with CO<sub>2</sub> from the air, and was catalyzed by water. The degradation destroyed the electrolyte disc, which then lost its electrochemical performance. Our results showed that both moisture and CO<sub>2</sub> were needed to start the degradation process. The absorbed water molecules facilitated the formation of Ba ions traps and the growth of BaCO<sub>3</sub> nano-rod single crystals directly from the BZCY surface. This occurred via the so-called ‘microcrucible mechanism’. The decomposition of BZCY also produced amorphous ZrO<sub>2</sub>, CeO<sub>2</sub> and Y<sub>2</sub>O<sub>3</sub>, and presumably Y<sub>2</sub>(OH)<sub>2</sub>(CO<sub>3</sub>)<sub>2</sub> as well. Each degradation cycle released one water molecule, so water was a true catalyst in this remarkable reaction. Interestingly, the degradation was fully reversible upon calcination at 1200°C. Nevertheless, to avoid electrochemical performance loss and unexpected additional complexities to the fuel cell system, we highly recommend that fabricated SOFCs containing doped barium cerate and/or zirconate components should be stored in a dry or CO<sub>2</sub>-free environment.

### Acknowledgments

N.Y., W.W., T.G., J.L.L acknowledge the Strategic Project Grant of Natural Sciences and Engineering Research Council (NSERC) of Canada. Part of this research was supported by the Research Priority Area Sustainable Chemistry of the University of Amsterdam, <http://suschem.uva.nl>. All authors gratefully acknowledge RIEM project from NSERC-MRS.

### References

1. M. C. Williams, J. P. Strakey, and W. A. Surdoval, *J. Power Sources*, **143**, 191 (2005).
2. H. A. Gasteiger and N. M. Markovic, *Science*, **324**, 48 (2009).
3. S. D. Park, J. M. Vohs, and R. J. Gorte, *Nature*, **404**, 265 (2000).
4. A. Atkinson, S. Barnett, R. J. Gorte, J. T. S. Irvine, A. J. McEvoy, M. Mogensen, S. C. Singhal, and J. Vohs, *Nat. Mater.*, **3**, 17 (2004).
5. W. Sun, M. Liu, and W. Liu, *Adv. Energy Mater.*, **3**, 1041 (2013).
6. J. G. Lee, J. H. Park, and Y. G. Shul, *Nat. Commun.*, **5**, 4045 (2014).
7. Y. Zhou, H. Wu, T. Luo, J. Wang, Y. Shi, C. Xia, S. Wang, and Z. Zhan, *Adv. Energy Mater.*, **5**, 1500375 (2015).
8. S. Sengodan, S. Choi, A. Jun, T. H. Shin, Y.-W. Ju, H. Y. Jeong, J. Shin, J. T. S. Irvine, and G. Kim, *Nat. Mater.*, **14**, 205 (2015).
9. I. W. Chen, S.-W. Kim, J. Li, S.-J. L. Kang, and F. Huang, *Adv. Energy Mater.*, **2**, 1383 (2012).
10. J. Mirzababaei, L.-S. Fan, and S. S. C. Chuang, *J. Mater. Chem. A*, **3**, 2242 (2015).
11. K. D. Kreuer, *Annu. Rev. Mater. Res.*, **33**, 333 (2003).
12. N. Yan, X.-Z. Fu, K. T. Chuang, and J.-L. Luo, *J. Power Sources*, **254**, 48 (2014).
13. G. Rothberg, E. A. de Graaf, and A. Blik, *Angew. Chem. Int. Ed.*, **42**, 3366 (2003).
14. J. Wu, L. P. Li, W. T. P. Espinosa, and S. T. Haile, *J. Mater. Res.*, **19**, 2366 (2004).
15. F. L. Chen, O. T. Sorensen, G. Y. Meng, and D. K. Peng, *J. Mater. Chem.*, **7**, 481 (1997).
16. A. Kruth, R. A. Davies, M. S. Islam, and J. T. S. Irvine, *Chem. Mater.*, **19**, 1239 (2007).
17. L. Yang, S. Wang, K. Blinn, M. Liu, Z. Liu, Z. Cheng, and M. Liu, *Science*, **326**, 126 (2009).
18. R. Kannan, K. Singh, S. Gill, T. Fuerstenhaupt, and V. Thangadurai, *Sci. Rep.*, **3**, 2138 (2013).
19. N. Zakowsky, S. Williamson, and J. T. S. Irvine, *Solid State Ionics*, **176**, 3019 (2005).
20. S. V. Bhide and A. V. Virkar, *J. Electrochem. Soc.*, **146**, 2038 (1999).
21. T. Tauer, R. O’Hayre, and J. W. Medlin, *Chem. Mater.*, **26**, 4915 (2014).
22. E. Fabbri, A. D’Epifanio, E. Di Bartolomeo, S. Licocchia, and E. Traversa, *Solid State Ionics*, **179**, 558 (2008).
23. F. M. M. Sniijkers, A. Buekenhoudt, J. Coymans, and J. J. Luyten, *Scripta Mater.*, **50**, 655 (2004).
24. E. Fabbri, D. Pergolesi, and E. Traversa, *Chem. Soc. Rev.*, **39**, 4355 (2010).
25. C. Zuo, S. Zha, M. Liu, M. Hatano, and M. Uchiyama, *Adv. Mater.*, **18**, 3318 (2006).
26. B. Lin, Y. Dong, R. Yan, S. Zhang, M. Hu, Y. Zhou, and G. Meng, *J. Power Sources*, **186**, 446 (2009).
27. X. Guo, *Chem. Mater.*, **16**, 3988 (2004).
28. S. Gopalan and A. V. Virkar, *J. Electrochem. Soc.*, **140**, 1060 (1993).
29. C. A. Traina and J. Schwartz, *Langmuir*, **23**, 9158 (2007).
30. E.-M. Koeck, M. Kogler, T. Bielz, B. Kloetzer, and S. Penner, *J. Phys. Chem. C*, **117**, 17666 (2013).
31. H. Kruidhof, H. J. M. Bouwmeester, R. H. E. Vondooorn, and A. J. Burggraaf, *Solid State Ionics*, **63-5**, 816 (1993).
32. I. Arvanitidis, D. Sichen, and S. Seetharaman, *Metall. Mater. Trans. B*, **27**, 409 (1996).
33. L. M. Dassuncao, I. Giolito, and M. Ionashiro, *Thermochim. Acta*, **137**, 319 (1989).
34. L. M. Dassuncao, M. Ionashiro, D. E. Rasera, and I. Giolito, *Thermochim. Acta*, **219**, 225 (1993).
35. D. Pergolesi, E. Fabbri, A. D’Epifanio, E. Di Bartolomeo, A. Tebano, S. Sanna, S. Licocchia, G. Balestrino, and E. Traversa, *Nat. Mater.*, **9**, 846 (2010).
36. T. Gougousi and Z. Chen, *Thin Solid Films*, **516**, 6197 (2008).
37. N. Yan, J.-L. Luo, and K. T. Chuang, *J. Power Sources*, **250**, 212 (2014).
38. C. C. Lundstrom, *Nature*, **403**, 527 (2000).
39. P. Babilo, T. Uda, and S. M. Haile, *J. Mater. Res.*, **22**, 1322 (2007).
40. A. A. Herzing, H. W. Ro, C. L. Soles, and D. M. Delongchamp, *ACS Nano*, **7**, 7937 (2013).
41. S. Kashyap, T. J. Woehl, X. Liu, S. K. Mallapragada, and T. Prozorov, *ACS Nano*, **8**, 9097 (2014).
42. I. Matsubara, R. Funahashi, T. Ogura, H. Yamashita, K. Tsuru, and T. Kawai, *J. Cryst. Growth*, **141**, 131 (1994).
43. R. Boston, Z. Schnepp, Y. Nemoto, Y. Sakka, and S. R. Hall, *Science*, **344**, 623 (2014).
44. K. D. Kreuer, *Chem. Mater.*, **8**, 610 (1996).
45. M. P. Delmo, S. Yamamoto, S. Kasai, T. Ono, and K. Kobayashi, *Nature*, **457**, 1112 (2009).
46. Y. Lin, S. Fang, D. Su, K. S. Brinkman, and F. Chen, *Nat. Commun.*, **6**, 6824 (2015).